ELSEVIER

Contents lists available at ScienceDirect

Journal of Hydrology

journal homepage: www.elsevier.com/locate/jhydrol



Research papers

A numerical exploration of hyporheic zone solute transport behavior estimated from electrical resistivity inversions

Xiaolang Zhang a,*, Audrey H. Sawyer , Kamini Singha b

- a School of Earth Sciences. The Ohio State University. Columbus. OH 43210. USA
- b Department of Geology and Geological Engineering, Hydrologic Science and Engineering Program, Colorado School of Mines, Golden, CO 80401, USA



An increasing number of studies have combined saline tracer injections with time-lapse electrical resistivity (ER) surveys to explore solute exchange within the hyporheic zone. The reliability and resolution of ER surveys of the hyporheic zone are rarely discussed. Here, we use a numerical modeling approach to assess how ER imaging resolves changes in saline tracer concentration within the hyporheic zone given different synthetic scenarios. We create a 3-D synthetic stream and surrounding hyporheic zone with an ER electrode transect and solve the coupled equations for porous fluid flow and solute transport. Then, we solve for the 3-D conduction of current between electrodes to create synthetic time-lapse ER surveys and invert the simulated resistances to obtain 2-D bulk electrical conductivity (σ_b) images perpendicular to the stream, which we compare with the known synthetic σ_b fields. The σ_b fields in the inversion generally capture the shape of the simulated σ_b fields, but with smoothing and artifacts as a function of the inversion process. Consequently, the calculated cross-sectional area of tracer plume is inaccurate. At inversion pixels beneath the stream, the accuracy of the inverted σ_b breakthrough curves when compared to the synthetic "truth" varies with stream size, pixel depth, and to a lesser extent injection time. The tails of these pixel breakthrough curves beneath the stream are consistently underestimated compared to the synthetic "truth," i.e., σ_b in the inversions appear to return to background faster by one to six hours. The time series of average apparent bulk electrical conductivity requires no inversion and captures lingering saline tracer better than bulk EC breakthrough curves at individual pixels in the inversions.

1. Introduction

The interaction between stream water and groundwater is complicated (Winter et al., 1998; Woessner, 2000; Lewandowski et al., 2020) due to site-specific heterogeneity in streambed permeability and timeand space-varying hydraulic gradients. Stream water-groundwater exchange, or hyporheic exchange, has been inferred from measurements of concentration breakthrough curves during tracer tests, either in streams or in monitoring wells (Hammett et al., 2022). Processes and parameters of interest such as exchange fluxes and residence times can be difficult to estimate from these data alone because: (1) tracer experiments are sensitive to more than just hyporheic exchange (Harvey et al., 1996); and (2) concentrations measured at one location in space give an integrated measure of what occurs upgradient and no information about variability along the transport pathway. Identifying hydrologic factors that control exchange over various spatial scales is critical for understanding patterns of water quality and ecological community structure (Triska et al., 1993; Wondzell and Swanson, 1996; Knapp et al. 2017). Temporal scales of exchange are also important, as daily to seasonal variations in flows may control transport behavior (Bryant et al., 2020; Wroblicky et al., 1998); however, few methods are available to quantify

the variations at the appropriate spatial and temporal scales.

Hydrogeophysical methods are a rapidly emerging tool to characterize and monitor hydrologic processes at spatial and temporal resolution heretofore impossible (e.g., Binley et al., 2015). In particular, time-lapse electrical resistivity (ER) imaging (recording electrical resistivity change with time) has provided high-resolution spatial and temporal information about transport of fluids and solutes in diverse geologic settings (Busato et al., 2019; Doetsch et al., 2012; Sawyer et al., 2015) and has been used extensively in hyporheic studies (summarized in Table 1). ER methods are used to estimate the distribution of bulk electrical resistivity (or its reciprocal, bulk electrical conductivity, denoted σ_b) of a medium by driving an electrical current between two source electrodes and measuring the resultant potential distribution at two or more receiver electrodes. The measured resistances are averages of the electrical properties of the porous media and conductive fluid in the system. Because ER methods are sensitive to changes in σ_h of the subsurface, ER has frequently been used to monitor spatial and temporal surface water-groundwater interactions from conductive tracer tests in stream systems. ER has been found to resolve targets from the sub-meter to tens-of-meters scale in the field depending on the support volume of measurements and tomographic resolution (Table 1). The resolution and

E-mail address: zhang.12842@osu.edu (X. Zhang).

^{*} Corresponding author.

support volume, however, are complicated functions of the σ_b distribution in the subsurface, the data acquisition geometry, and data noise (Daily and Ramirez, 1995; Day-Lewis et al., 2005). These properties affect the subsequent ER inversions, which are generally too smooth, underestimate high values and overestimate low ones, and show lower resolution far from the electrodes (Day-Lewis et al., 2005). Consequently, mapping the mass or volume of conductive targets using ER is difficult. For example, large, diffuse targets may be more detectable than small, concentrated plumes (Singha and Gorelick, 2005; Bethune et al. 2015).

Despite these limitations, many researchers have been interested in using ER to monitor changes in the hyporheic exchange zone (e.g., Ward et al., 2010; Smidt et al., 2015; Sparacino et al., 2019) (Table 1), which varies in time and space (Boano et al., 2008; Gooseff et al., 2006). For example, Ward et al. (2012) used ER inversions to show that hyporheic extent decreased with baseflow recession, in contrast to expectations from some conceptual models (e.g., Hakenkamp et al., 1993; White, 1993). One important caveat is that estimating a quantitative change in hyporheic extent (or size of a saline tracer plume) requires the selection of a meaningful change in inverted bulk conductivities $\sigma_{b,i}$ between inversions in time, which makes the analysis subjective.

Because inversions are affected by smoothing and artifacts as noted above, another useful measurement of change within the system is to look at the data themselves, e.g., the apparent bulk electrical conductivity ($\sigma_{b,a}$) (e.g., Coscia et al., 2011; Dehkordy et al., 2019; Doughty et al., 2020). For example, Coscia et al. (2011) showed reasonable agreement between the tail of the $\sigma_{b,a}$ measured from ER, and fluid electical conductivity (EC) from nearby piezometers that were screened through the ~4-m thick saturated aquifer. One issue with these $\sigma_{b,a}$ data, however, is that they are volumetric averages of the system through which the current flows, and consequently are not indicative of change in any specific region of interest in the subsurface. Consequently, $\sigma_{b,i}$ are needed to get spatially distributed information.

In addition to the noise and unreliability introduced via smoothing

and artifacts during ER inversions, the size of the stream-hyporheic system and the experimental design likely influence the ability of ER inversions to resolve changes in saline tracer extent. For example, because the stream is a zone of high EC that lies immediately above the hyporheic target, changes in saline tracer concentration in overlying surface water may be challenging to disentangle from changes in saline concentration in the hyporheic zone using ER inversions alone. Previous research has explored steps to try to mitigate these effects, such as separating the stream from the aquifer during regularization of the inverse problem, and/or assuming known stream bathymetry and changes in stream water EC (e.g., Coscia et al., 2011; McLachlan et al., 2021). These techniques are undoubtedly necessary in large streams to obtain accurate estimates of subsurface characteristics but may be harder to implement in some of the shallow, first-order streams where many hyporheic studies are conducted (Table 1) because to resolve stream bathymetry at high resolution is computationally expensive. To make pixel resolution of inversion fine enough in small streams, the size of electrodes may be comparable to the pixel size, and the impacts of electrodes themselves on the inversion may be exemplified. These complications may limit the extent to which we can trust the spatial and temporal information that ER surveys give us about the hyporheic zone.

Here, we look to explore how tracer injection design and stream characteristics affect the reliability of ER surveys in a controlled system. To do so, we create a set of 3-D finite-element models. In our synthetic models, stream tracer tests are coupled with ER surveys, and the synthetic resistance data (converted to $\sigma_{b,a}$) are then inverted in 2-D following standard methods to compare the known σ_b with $\sigma_{b,i}$ and $\sigma_{b,a}$. Specifically, we explored three primary issues: 1) stream area or size, 2) injection concentration, and 3) injection times. We chose to examine stream area because the stream is a highly electrically conductive feature that lies immediately above the target feature (the hyporheic zone), and we sought to understand how its size influences the quality of the inversion in the target zone. We examined injection concentration and injection time to explore whether feasible adjust-

Table 1 Summary of time-lapse ER studies focused on surface water-groundwater interactions. Fluid EC values with asterisk (*) indicate measurements in a borehole near the injection location rather than surface water. Types of analysis are as follows: 0 = ER inversions and qualitative interpretation, $1 = \bar{\sigma}_{b,a}$, $2 = \sigma_{b,i}$ breakthrough curves, 3 = temporal moment calculation from breakthrough curves ($\bar{\sigma}_{b,a}$ or $\sigma_{b,i}$), 4 = saline tracer plume area using threshold change in EC.

Reference	Injection Time (h)	Injection Location	Fluid EC: Initial, Peak (uS/cm)	Channel Width (m)	Channel Depth (m)	Stream Discharge (L/s)	Analysis	Notes
(Ward et al., 2010a)	20.8	stream		2	0.1	0.6	0,4	
(Ward et al., 2010b)	3	stream	5,002,000	2		170	0,1,3	synthetic
(Cardenas and Markowski, 2011)	n/a	none	650	60	0.7		0	natural tracer
(Coscia et al., 2011)	n/a	none	450,360*	40		$2.5 \times 10^4 - 7.5 \times 10^5$	0,1	natural tracer
(Doetsch et al., 2012)	0.333	borehole (bank)	500,7800*	$10^1 - 10^2$			0	
Toran et al., 2012)	2	stream	400,850	3	0.1	28	0	
(Ward et al., 2012)	48	stream	40	4	0.45	4–35	0,2,4	
(Larson et al., 2013)	10	stream	1,800,600	8		7.8	0,2	dilution tracer
(Toran et al., 2013)	2	stream	400,750	3	0.1	38	0	
(Menichino et al., 2014)	6.5	borehole (bank)	$10^3, 10^{4*}$	0.6	0.2	10	0	
Ward et al., 2014)	48	stream	40,140	4	0.45	4–35	0,3	
(Gonzalez-Pinzon et al., 2015)	2.8	stream	90,155	1.0-2.0		206	0,2	
Johnson et al., 2015)	n/a	none	400,150	102		$10^6 - 10^7$	0,2	natural tracer
(Sawyer et al., 2015)	0.75	karst window	610,760*			700	0,2	
(Smidt et al., 2015)	4.7	stream	228, 368	10	0.25	260	0,2,3,4	
(Clemence et al., 2017)	1.5	streambed	450,460*	1	0.1		0	
(Dehkordy et al., 2019)	10	streambed	900,2500*	1.9	0.09	1200	0,1	
(Busato et al., 2019)	n/a	none	30, 40	15			0,2	natural tracer
(Sparacino et al., 2019)	4	stream	30,130	1.6	0.4	65	0	
(Doughty et al., 2020)	4	stream	20,80	6	0.15-0.35	17–760	0,1,3	
(Houzé et al., 2022)	1	stream	18.82, 82.56	4	1	170	0	

ments to the duration of the injection or peak concentration could improve the detection of tracer in the hyporheic zone downstream. Our goal is to provide suggestions for designing time-lapse ER surveys of hyporheic zones in the field and guidelines to improve the interpretation of ER inversion results, specifically how hyporheic area and the spatial distribution and timing of solute arrival and flushing in the hyporheic zone are interpreted using ER inversion results.

2. Methods

Our objective is to use a numerical modeling approach to explore the performance of time-lapse ER surveys for quantifying hyporheic solute transport. Because these studies are generally conducted in relatively small streams where a continuous injection of saline tracer is feasible (e. g. Ward et al., 2010a; Toran et al., 2013; Gonzalez-Pinzon et al., 2015), we limit our analysis to scenarios with relatively shallow streams. Threedimensional fluid flow, solute transport, and electrical conduction are simulated for a stream and the surrounding porous medium during and after the injection of a saline tracer solution. A two-dimensional ER survey profile is set perpendicular to the stream in the model domain, and voltages at 12 electrodes are modeled in response to a sequence of currents. The synthetic $\sigma_{b,a}$ measurements are then inverted to create maps in $\sigma_{b,i}$, which can be compared with known changed in σ_b as a test of interpretation pitfalls. We performed this analysis for three scenarios with various stream sizes (0.1 m deep \times 4 m wide, 0.2 m deep \times 6 m wide, and 0.3 m deep $\times 8 \text{ m}$ wide). Because of the long run times of our simulations, we took advantage of the fact that stream width and depth tend to scale with one another in natural streams (Allen et al., 2018), and we increased width and depth together. We also tested different tracer injection designs (injection time for 4, 6, and 8 h; injection concentration 0.2, 0.3, and 0.4 mS cm⁻¹). Finally, we tested one scenario with heterogeneous sediment permeability to explore how irregular features of the tracer plume are resolved in ER inversions. The base case has a stream geometry of 0.2 m deep \times 6 m wide, an injection time of 6 h, an injection concentration of 0.3 mS cm⁻¹, and homogeneous sediment (Table 2). We did not test parameters related to ER survey design such as number and spacing of electrodes, which have been examined previously (Wilkinson et al., 2006; Ward et al., 2010b).

2.1. Numerical modeling of a homogeneous hydraulic conductivity system

Three-dimensional finite-element models of a stream-aquifer system were constructed using COMSOL Multiphysics (COMSOL Multiphysics,

Table 2Model parameters. Bold indicates variables in synthetic experiments. Asterisk (*) denotes value in base scenario (Section 3.1).

Symbol (Units)	Value	Definition
$D_D (\mathrm{m}^2 \mathrm{s}^{-1})$	3×10^{-6}	Dispersion coefficient
$De (m^2 s^{-1})$	5×10^{-11}	diffusion coefficient
$D_{\rm s}~({\rm m}^2~{\rm s}^{-1})$	0.5	in-stream dispersion coefficient
d_s (m): w_s (m)	0.1:4, 0.2:6*,	stream depth:width
	0.3:8	
$K (\text{m s}^{-1})$	2×10^{-3}	aquifer hydraulic conductivity
L (m)	1.2	distance from injection to ER survey line
$t_{I}(\mathbf{h})$	4, 6*, 8	injection duration
$v_s (m s^{-1})$	0.1	in-stream velocity
$\alpha (h^{-1})$	0.01	mobile-immobile transfer coefficient
$\theta_i(-)$	0.1	immobile porosity
$\theta_m(-)$	0.2	mobile porosity
$_{\sigma s,}$ (mS cm ⁻¹)	0.1	initial fluid conductivity in stream
$_{\sigma s,p}({ m mS~cm}^{-1})$	0.2, 0.3*, 0.4	plateau fluid conductivity in stream
$_{\sigma f_s}$ (mS cm ⁻¹)	0.15	fluid conductivity in groundwater
		endmember
h_a (m)	0.002	amplitude of hydraulic head variations
L_1 (m), L_2 (m)	0.5, 2	length scales of bedforms
T_1 (m), T_2 (m)	0.1, -0.1	Lateral offsets in bedform crest positions

2019). The model represents three sets of governing physics: (1) steady-state fluid flow in porous media, (2) transient solute transport, and (3) steady-state electrical conduction. The synthetic study reach was designed to be a simplified version of a typical mountain stream, which is inspired by work conducted at Watershed 03 at the H.J. Andrews Experimental Forest. All synthetic ER surveys were conducted with 12 electrodes spaced 1 m apart and 317 combinations of current source-sink and measurement electrodes in a dipole-dipole configuration (similar to Ward et al., 2010). We focus on a dipole-dipole geometry because it usually generates the fastest data collection with most available ER systems, and speed of ER data collection is a particularly important requirement in fast-moving stream systems to avoid temporal smearing. There is consequently a trade-off in the field between speed of data collection and collecting enough data to make quality inversions; dipole-dipole is one of the best geometries to manage this issue.

The model geometry was composed of two domains: stream and porous aquifer. To minimize the calculation cost, porous fluid flow and saline tracer transport were only simulated in the portion of the aquifer near the stream and electrode transect because fluid EC and thus σ_h do not vary beyond the hyporheic zone over the timescale of tracer injections (Fig. 1a). Electrical conduction was simulated over a larger domain (that includes areas of constant σ_h) far from the stream to minimize boundary effects on electrical currents. As noted above, stream sizes were varied from 4 m wide and 0.1 m deep to 8 m wide and 0.3 m deep (Table 2), with a base case scenario of 6 m wide and 0.2 m deep. The portion of the aquifer near the stream extended 2.4 m from the stream sides on either side and 2 m below the stream bottom. The entire aquifer zone was 100 m wide, 100 m deep, and 100 m long (extended 50 m upstream and downstream from the electrode transect) to minimize boundary effects on electrical conduction near the electrodes. The saline tracer injection location was positioned 50 m upstream from the electrode transect to ensure adequate mixing of salt to depth at the electrode transect. At the injection, the saline tracer was instantaneously wellmixed across the entire stream cross-section. To resolve fine changes in solute concentration around the electrode transect, the finite-element model grid spacing along the stream was set to less than 0.03 m in the downstream direction and 0.015 m in the vertical direction.

The steady-state groundwater flow equation was first solved for the aquifer near the stream (Fig. 1a):

$$\nabla(K\nabla h) = 0 \tag{1}$$

where K is the hydraulic permeability (m s⁻¹), and h is hydraulic head (m). The floodplain surface was specified as a no-flow boundary (zero net recharge). At the upstream and downstream faces, influx and efflux rates were chosen to be consistent with the hydraulic conductivity of the aquifer and the down-valley hydraulic head gradient (J) was assumed to be 0.01 m m⁻¹, representative of moderate to steep small-order streams. In addition, the lateral sides and base of the domain were assigned the same down-valley slope (J) in hydraulic head but raised uniformly by an additional 0.1 mm relative to the stream to generate a weakly gaining stream condition, or slow groundwater flow towards the stream. We created a weakly gaining stream for model convenience— to reduce the effect of domain size on the steady-state fluid EC field in the hyporheic zone—but our findings are equally applicable to neutral or losing systems. The sediment-water interface was assigned a non-uniform hydraulic head condition, $-Jx + h_{bed}(x,y)$, to represent the interactions of currents with a rough bed (e.g. Elliott and Brooks, 1997, Stonedahl et al., 2010) (Fig. 1c), where:

$$h_{bed}(x,y) = h_a \cos\left[\frac{2\pi}{L_1} \left(x - T_1 \sin\left(\frac{2\pi}{L_2}y\right)\right)\right] - h_a \sin\left[\frac{2\pi}{L_2} \left(x\right)\right] - T_2 \cos\left(\frac{2\pi}{L_2}y\right)\right]$$
(2)

 h_a is the amplitude of hydraulic head variations along the stream associated with bedforms of length scale L_1 and L_2 . T_1 and T_2 are lateral

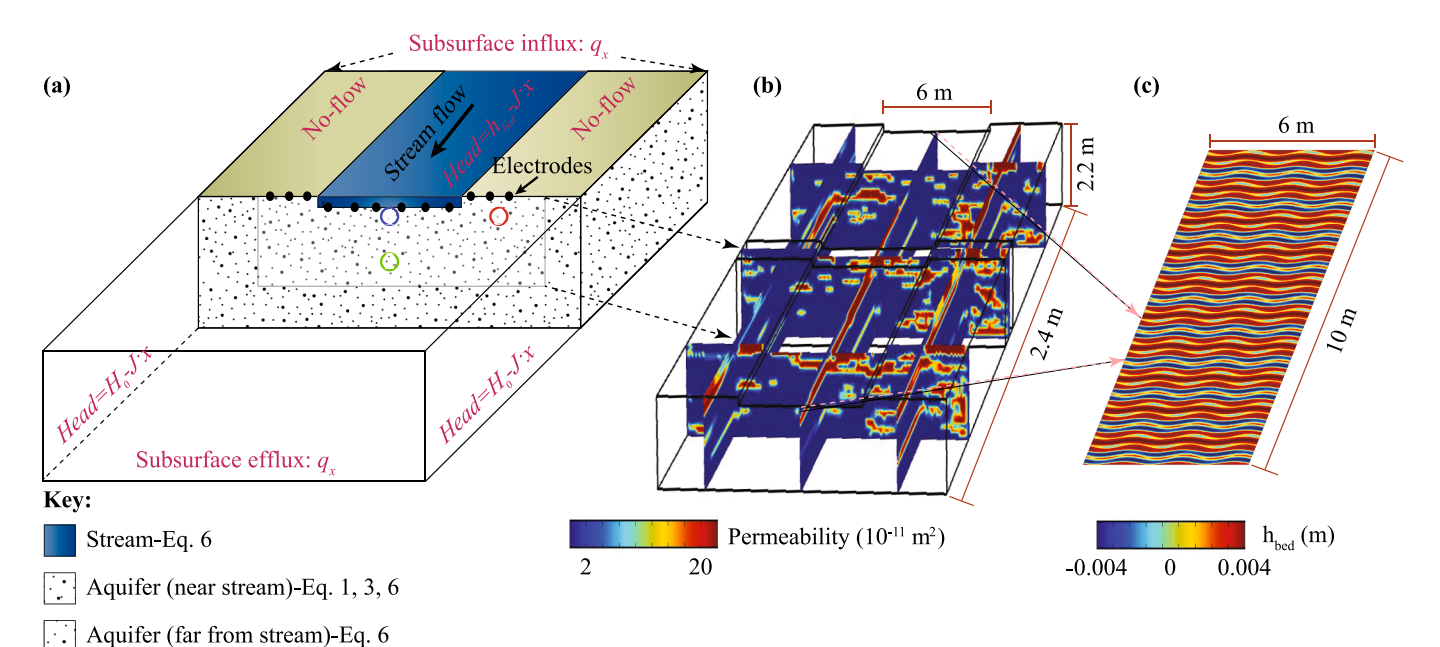


Fig. 1. A) model geometry in comsol. steady groundwater flow (equation(1) and transient solute transport (Equations (3a)-b) are only solved in the near-stream region (white stippled area). The subsurface boundary conditions are shown in orange text. $J = 0.01 \text{ m m}^{-1}$, $q_x = 2 \times 10^{-5} \text{ m s}^{-1}$, and $H_0 = 0.0001 \text{ m}$. Steady electrical conduction (Eq. (6) is solved in all regions. The space only for electrical conduction is not thoroughly shown due to it being too large. Spacing between electrodes is 1 m. Locations of three pixel-breakthrough curves (labeled 1–3 in subsequent figures) are shown in blue, green, and red. b) Bimodal permeability field used in heterogeneous scenario. c) Prescribed variations in hydraulic head due to bedform-current interactions (h_{bed} , Eq. (2). (For interpretation of the references to colour in this figure legend, the reader is referred to the web version of this article.)

offsets in the bedform crest locations (Table 2). The hyporheic exchange patterns and rates that result from this non-uniform hydraulic head condition are three-dimensional with the greatest hyporheic velocities in the downstream direction

The velocity fields from the steady groundwater-flow solution were used to solve for conservative tracer transport in the hyporheic zone based on the transient advection-dispersion equation with exchange between mobile and immobile pores:

$$\theta_m \frac{\partial c_m}{\partial t} + \theta_i \frac{\partial c_i}{\partial t} = -\theta_m \mathbf{u} \bullet \nabla c_m + \theta_m (D_D + D_e) \nabla^2 c_m$$
(3a)

$$\theta_i \frac{\partial c_i}{\partial t} = \alpha(c_m - c_i) \tag{3b}$$

where subscript m denotes the mobile domain and i denotes the immobile domain. θ (–)is porosity, c (mS cm⁻¹) is the solute concentration in the pore space, t (s) is time, D_D (m² s⁻¹) is the coefficient of hydrodynamic dispersion, D_e (m² s⁻¹) is the diffusion coefficient, \boldsymbol{u} (m s^{-1}) is the seepage velocity vector, and α (s^{-1}) is a mass transfer coefficient between mobile and immobile pores (Table 2). A dual-domain model with mobile and immobile pores in the aquifer was chosen over a single-domain model to better represent the persistence of tracer in pore spaces long after the bulk of tracer mass has been flushed from the stream (Ward et al., 2010b). The "solute" used to represent the saline tracer was fluid EC, which has units of mS cm⁻¹ rather than concentration units since fluid EC travels conservatively and maintains a linear relationship with tracer concentration. Concentration within the stream and along the sediment-water interface (c_s, mS cm⁻¹) was specified based on the Ogata solution for a tracer injection with initial in-stream concentration c_0 (mS cm⁻¹), in-stream plateau concentration c_n (mS cm⁻¹), average longitudinal stream-water velocity v_s (m s⁻¹), in-stream dispersion coefficient D_s (m² s⁻¹), injection interval t_I (s), and distance L(m) between the ER transect and the upstream injection location:

$$c_{s}(t) = c_{0} + \frac{(c_{p} - c_{0})}{2} \left[erfc\left(\frac{L - v_{s}t}{2\sqrt{D_{s}t}}\right) + exp\left(\frac{v_{s}L}{D_{s}}\right) erfc\left(\frac{L + v_{s}t}{2\sqrt{D_{s}t}}\right) \right] - \frac{(c_{p} - c_{0})}{2} \left[erfc\left(\frac{L - v_{s}(t - t_{I})}{2\sqrt{D_{s}(t - t_{I})}}\right) + exp\left(\frac{v_{s}L}{D_{s}}\right) erfc\left(\frac{L + v_{s}(t - t_{I})}{2\sqrt{D_{s}(t - t_{I})}}\right) \right]$$

$$(4)$$

A constant background concentration for a groundwater endmember, c_g (mS cm $^{-1}$), was assumed along the sides and bottom of the aquifer region near the stream (Fig. 1a, Table 2). The land surface or top of the aquifer outside the stream was treated as a zero-flux boundary. The initial concentration (or fluid EC) field was specified from the steady solution to Eq. (4). Transient solutions for fluid EC (Eq. (4) were retained at 15-minute intervals to simulate time-lapse ER surveys at those times.

To convert fluid EC fields at each time step to σ_b , we used a simple petrophysical model from Singha et al. (2007)

$$\sigma_b = (\theta_m + \theta_i)^{m-1} (\theta_m \sigma_{f,m} + \theta_i \sigma_{f,i})$$
(5)

where m is the cementation exponent equal to 1.3 and $\sigma_{f,m}$ (mS cm⁻¹) and $\sigma_{f,i}$ (mS cm⁻¹) are the fluid EC values for the mobile and immobile pore spaces, respectively. This model assumes that the fluids in mobile and immobile pore spaces behave as conductors in parallel; Additionally, surface conductance is ignored. Stream EC was converted directly to σ_b given a porosity of 100%.

The calculated σ_b fields were then used to simulate resistance values at the electrodes that would be measured by ER instrumentation in the field by solving the Poisson equation for electrical conduction:

$$\nabla h(\sigma_h \nabla V) = -I\delta(x, y) \tag{6}$$

where V(V) is electric potential, and I(A) is the magnitude of the current source applied at electrodes, and resistance is defined by $\Delta V/I$ between two electrodes. The ground and water surfaces were treated as insulation boundaries, while the sides and base of the model were zero-voltage boundaries. To create the synthetic ER survey data, we solved Eq. (6) once for each electrode (12 times) at each time step, where we

applied a current source at the electrode of interest and extracted the voltages at the remaining electrodes. We then used the law of superposition to calculate 317 combinations of resistance readings, according to the electrode sequence, at each time step. Random 2% Gaussian noise was added to the modeled resistances to represent the typical magnitude of noise in field surveys. In real ER surveys, the sequence of current induction and voltage readings often spans minutes, during which time changes in the σ_b field may have occurred as the tracer migrated. In this synthetic ER survey, the sequence is effectively instantaneous because all resistances are "measured" within the same σ_b field. As such, the synthetic survey does not include the effects of temporal smearing that may occur in real ER surveys.

For each time step in a synthetic survey, we computed $\sigma_{b,a}$ for each combination in the electrode sequence. $\sigma_{b,a}$ is the equivalent bulk conductivity of a homogeneous earth given a measured $\Delta V/I$:

$$\sigma_{b,a} = I/GV \tag{7}$$

where

$$G = \frac{2\pi}{\frac{1}{OM} - \frac{1}{ON} - \frac{1}{TM} + \frac{1}{TN}}$$
 (8)

G (–) is a geometric factor, where $O\bar{M}, O\bar{N}, P\bar{M}$, and $P\bar{N}$, are the distances between electrodes O and M, O and N, P and M, and P and N, respectively. We then computed the average of the 317 $\sigma_{b,a}$ values at each time step to construct a breakthrough curve of $\bar{\sigma}_{b,a}$. The $\bar{\sigma}_{b,a}$ breakthrough curve allows us to quantify changes in bulk electrical conductivity over time without the complications of regularization from inversion, but these measurements do not have true locations in space as they are effective properties over the paths of the current, which depends on the σ_b of the system. We compared the $\bar{\sigma}_{b,a}$ changes with those of spatially averaged, known bulk $\bar{\sigma}_b$ in the synthetic stream system, evaluated across the vertical cross-section through the stream and near-stream aquifer regions at the ER transect location, which has cross-sectional area A_T :

$$\bar{\sigma}_b = 1/A_T \iint \sigma_b dx dz \tag{9}$$

where x- and z-axis are transversely and vertically perpendicular to the stream, respectively. This calculation of $\bar{\sigma}_b$ is valuable for understanding how the salt plume moves through the 2-D cross-section where the electrodes are located. It is related, but not equivalent to, the flux of saline tracer through the cross-section. The flow of current is 3-D in our models, but variations in salinity gradients along the stream are minor, so changes in $\bar{\sigma}_b$ can be reasonably captured in 2-D for comparison to $\sigma_{b,a}$. Exceptions may occur during two periods lasting a few minutes (much less than the survey interval of 15 min) at the start and end of the injection while the front of the tracer plume arrives in the stream at the transect location and while the tail passes, respectively.

2.2. Heterogeneous hydraulic conductivity case

To test the effects of a more irregular pattern of saline tracer spreading on inversion images, we also created a single test case with strong heterogeneity in hydraulic conductivity within the aquifer near the stream (Fig. 1b). It is important to note that we did not vary mobile or immobile porosity in this heterogeneous model—only hydraulic conductivity, which influences σ_b through its effect on flow and thus salt transport in the streambed. The bimodal hydraulic conductivity field consisting of sand and gravel lenses was simulated using TPROGS (Carle, 1999), which calculates the spatial attributes of geologic units using a Markov chain approach and indicator simulation with quenching. The volume of fine sand strata ($K = 2 \times 10^{-4} \text{ m s}^{-1}$) in the aquifer was 4 times of that of coarse sand strata ($K = 2 \times 10^{-2} \text{ ms}^{-1}$). The Markov chain approach characterizes fine-sand strata with mean length L_i (i

represents \times ,y, and z directions), based on transition probability $1/L_i$ between facies. L_i is an indicator of connectivity. A larger L_i value means that fine-sand strata are continuously distributed over a longer distance. L_i of fine-sand was 2, 0, and 0.1 m respectively, in downstream, channel-perpendicular, and vertical directions (x, y, and z). Fluid flow, solute transport, and electrical conduction were solved according to the same steps in Section 2.1.

2.3. Geophysical inversions

Synthetic ER survey data were inverted using the freely available software R2 (https://www.es.lancs.ac.uk/people/amb/Freeware/freew are.htm) using an algorithm based on Occam's inversion (Binley and Kemna, 2005). R2 searches for the best $\sigma_{b,i}$ model that matches the observed data (in a least-squares sense) in an iterative manner. For our models, we use the commonly adopted isotropic smoothness regularization. Given the small size of the synthetic stream, which is intended to represent 1st or 2nd order streams, we did not break it out separately from inversion, as has been done in field studies for larger streams (Table 1). An inversion was performed on the background dataset, and then subsequent data were inverted using the time-lapse differenceinversion approach of LaBrecque and Yang (2001). Inversions were acceptable when the root-mean-squared error between the true "data" and model-simulated data, normalized by the noise, approached unity. We consider changes in $\sigma_{b,i}$ greater than 2% (the applied noise) to be meaningful.

We compared the inferred changes in $\sigma_{b,i}$ at three model pixels in the hyporheic zone with known changes in σ_b within the synthetic stream system, also referred to as "reality" (Fig. 1a). The three pixels are positioned at three locations intended to represent a shallow hyporheic location that is well-connected to the overlying channel, a deeper location that is less hydrologically connected to the channel, and a location outside the stream in the bank beneath the electrode transect. Specifically, Location 1 is located 12.5 cm off the stream center and 15 cm below the sediment-water interface, Location 2 is located 12.5 cm off the stream center and 95 cm below the sediment-water interface, and Location 3 is located 187.5 cm outside the stream edge and 15 cm below the land surface interface. These places were selected based on where it would be reasonable to look for tracer to appear in a field setting, assuming no other knowledge from prior experiments. Therefore, comparing $\sigma_{b,i}$ with σ_b at these three locations should illustrate potential interpretation pitfalls; for example, scenarios where the inversion indicates a faster tracer arrival than the "real" arrival in the simulation. We also estimated the area of the saline tracer plume for the base case scenario to show difficulties in estimating this parameter meaningfully. The areas were defined by locations where the percent increase in σ_{hi} exceeded some thresholds change over background, as is often done in the literature. In this work, the actual decision of a threshold was not particularly important, as we just aimed to compare the inferred plume area in the inversion with the known area in the synthetic system, or "reality." We selected two thresholds of 5% and 10%. Because we focused on 2-D inversions, we did not estimate mass of tracer from the inversions, as has been done in 3-D efforts (e.g., Singha and Gorelick,

3. Results

3.1. Base scenario

3.1.1. $\bar{\sigma}_b$ and $\bar{\sigma}_{b,a}$

In the base scenario (Fig. 2a), fluid EC in the stream increases from 0.1 mS cm⁻¹ to 0.3 mS cm⁻¹, within the first 30 min of the injection and rapidly declines to the background value 6.5 h into the experiment, or 0.5 h after the end of the injection (Fig. 2a). The breakthrough curves in $\bar{\sigma}_{b,a}$ and $\bar{\sigma}_b$ both increase gradually over the duration of the injection, as

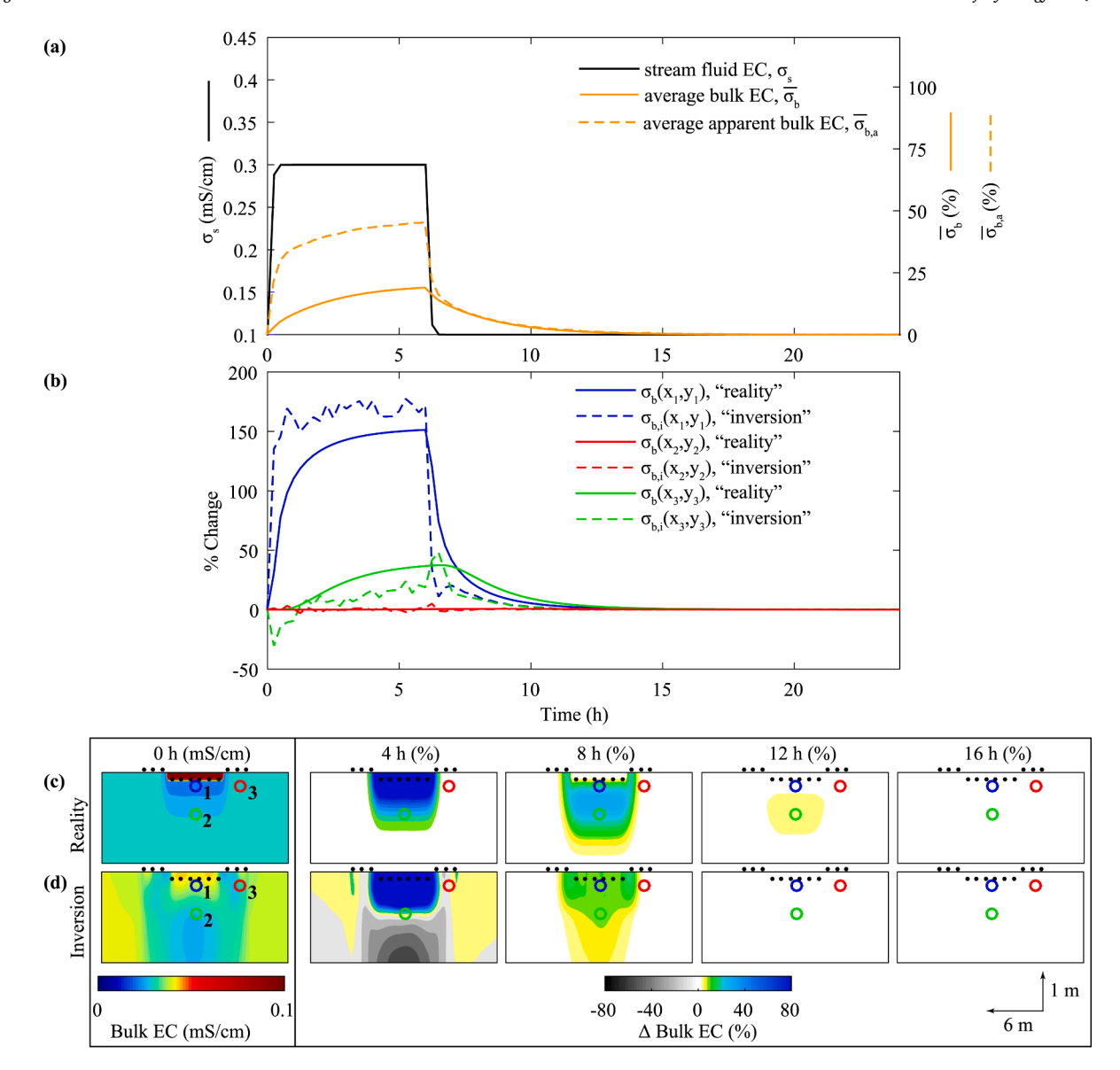


Fig. 2. Base scenario (denoted by asterisk in Table 1). a) Time series of stream fluid EC (σ_s) (solid black line), spatially averaged bulk EC ($\bar{\sigma}_b$, Eq. (9) over time in a cross-section beneath the electrode transect (solid orange line) and change in average apparent bulk EC ($\bar{\sigma}_{b,a}$) (Eq. (7), dashed orange line). b) Bulk EC at locations 1–3 for model ("reality", σ_b), solid line) and inversion ($\sigma_{b,i}$), dashed line). c-d) Bulk EC fields for model ("reality", σ_b) and inversion ($\sigma_{b,i}$), with the three monitoring locations shown. Timestep 0 h shows the background inversion, and later timesteps are the product of time-lapse inversions from the background. Areas in white indicate +/- 2%. (For interpretation of the references to colour in this figure legend, the reader is referred to the web version of this article.)

the hyporheic zone fills with tracer, and have lower magnitudes than the fluid EC, as expected, and they also show different magnitudes from one another (Fig. 2a). The magnitudes depend arbitrarily on the choice of averaging areas (for $\bar{\sigma}_b$) and electrode configurations (for $\bar{\sigma}_{b,a}$), and need not agree, but the shape of the tails holds important information about the passage of saline tracer. In this respect, the shape of the tails is similar, at least when compared to the fluid EC. A comparison between $\bar{\sigma}_{b,a}$ (Eq. (7), dashed orange line in Fig. 2a) and $\bar{\sigma}_b$ in a transect beneath the electrodes (Eq. (9), solid orange line in Fig. 2a) shows that both decay to 2% of the background value around 11.0 h (Table 3).

3.1.2. Inversions

In the synthetic hyporheic system ("reality"), most of the saline tracer remains confined to a region approximately 1 m from the sediment-water interface during the 6-hour injection period (Fig. 2c). After the injection ends and saline tracer has been flushed from the stream, a diffuse region of elevated σ_b remains within the hyporheic zone and expands outward ~ 1.5 m from the stream at 8 h. By 12 h, the

plume decreases in concentration, and the change in σ_b falls below 5% (Fig. 2c). The inversion results generally capture the geometry of the synthetic saline plume at 4 and 8 h with inversion effects (Fig. 2c and d). Namely, the change in $\sigma_{b,i}$ is underestimated in the highest σ_b areas of the plume, and there is an apparent decrease in $\sigma_{b,i}$ below the core of the plume that is not real (Fig. 2d). At later times after 8 h, $\sigma_{b,i}$ continues to underestimate the greatest changes in σ_b (Fig. 2d).

Examining the three individual pixel locations in the hyporheic zone (Fig. 2b), the changes in the system estimated $\sigma_{b,i}$ are generally similar to the "true" σ_b but decrease too rapidly at the end of the injection. At Location 1 (0.15 m deep in the streambed), σ_b in the synthetic system gradually increases over a period of 6 h. In comparison, $\sigma_{b,i}$ at Location 1 rapidly increases within the first 45 min and then generally plateaus until the end of the injection. The breakthrough curve reaches a slightly greater plateau in $\sigma_{b,i}$ than in σ_b at this location (Table 3). After the injection ends, σ_b declines to 10% of the background value after 8 h and obtains the background value after 11.8 h in the synthetic system

Table 3 Description of maximum % change and recovery time in: average apparent bulk EC $(\bar{\sigma}_{b,a})$ aerially averaged bulk EC in "reality" $(\bar{\sigma}_b)$, inverted bulk EC $(\sigma_{b,i})$ at discrete pixel locations, and bulk EC in "reality" (σ_b) at corresponding locations. When the matrix is within the 2% of background, the time to 2% is not available (N.A).

		Location 1		Location 2		Location 3		$\bar{\sigma}_b$	$\bar{\sigma}_{b,a}$
		$\sigma_{b,i}(\mathbf{x}_1,\mathbf{y}_1)$	$\sigma_b(\mathbf{x}_1,\mathbf{y}_1)$	$\sigma_{b,i}(\mathbf{x}_2,\mathbf{y}_2)$	$\sigma_b(\mathbf{x}_2,\mathbf{y}_2)$	$\sigma_{b,i}(\mathbf{x}_3,\mathbf{y}_3)$	$\sigma_b(\mathbf{x}_3,\mathbf{y}_3)$		
Maximum change (%)	Base scenario	177.4	151.2	48.2	37.4	4.9	0.6	17.4	41.5
	Small channel (4 m)	178.2	151.2	19.9	28.9	4.0	0.5	14.0	13.7
	Large channel (8 m)	139.3	151.3	48.1	48.4	1.7	0.7	19.7	62.7
	Dilute injection (0.2 mS cm ⁻¹)	79.6	75.6	11.0	18.7	2.0	0.3	8.7	18.9
	Concentrated (0.4 mS cm ⁻¹)	287.6	226.9	54.2	56.3	5.6	0.9	26.1	63.7
	Short injection (4 h)	177.9	147.5	55.4	33.2	5.9	0.5	15.6	39.7
	Long injection (8 h)	181.0	152.5	50.6	39.2	5.8	0.7	18.1	42.3
	Heterogenous	186.2	175.6	51.6	49.0	3.7	0.6	14.6	46.0
Time (h) to return to 2%	Base scenario	10.2	11.8	10.2	13.0	6.4	N.A.	10.7	11.0
	Small channel (4 m)	10.5	11.8	10.2	13.0	6.0	N.A.	10.0	10.0
	Large channel (8 m)	9.9	11.8	10.2	13.0	N.A.	N.A.	10.9	11.2
	Dilute injection (0.2 mS cm ⁻¹)	8.7	10.5	8.6	11.6	N.A.	N.A.	9.2	9.3
	Concentrated (0.4 mS cm ⁻¹)	10.9	12.6	11.1	13.9	7.3	N.A.	11.5	11.9
	Short injection (4 h)	7.9	9.6	8.0	10.8	4.5	N.A.	8.4	8.7
	Long injection (8 h)	12.2	13.9	12.3	15.1	8.5	N.A.	12.8	13.2
	Heterogenous	9.6	10.5	9.7	15.3	6.8	N.A.	11.0	10.7

(Fig. 2b). Meanwhile, $\sigma_{b,i}$ declines faster, reaching 10% of background within 8 h and obtaining its background value 10.2 h into the experiment (Fig. 2b, Table 3). At Location 2 (depth of 0.95 m in the streambed), tracer arrival is slower than at Location 1 in both $\sigma_{b,i}$ and σ_b . Some tracer arrives within 15 min in the synthetic system, and σ_b slowly climbs over the entire 6-hour injection period (Fig. 2b). Meanwhile in the inversion, artifacts cause an initial decrease in $\sigma_{b,i}$ within the first hour, followed by a gradual increase with a peak change of 48% at 6.5 h. σ_b decreases to 10% of the background value at 10 h in the synthetic simulation and 7.8 h in $\sigma_{b,i}$. At Location 3 (within the floodplain), the simulated σ_b change is less than 0.6%, in general agreement with $\sigma_{b,i}$ (all times except one have a change of less than 2%) (Table 3). It is impractical to visualize the mismatch everywhere in the inversion for all times, so we have selected these three locations as examples, but other points within the ER profile can be inferred from the changes in $\sigma_{b,i}$ and σ_h fields (Supplementary Figs. S1 – S4).

Plume areas estimated by inversion agree poorly with the simulated "reality" for either choice of threshold change (5% or 10%, Fig. 3), but

relative changes from timestep to timestep appear reasonable. In the case of the 10% threshold, the simulated plume area expands to 2.7 m² in the first 15 min of the test as tracer floods the stream (Fig. 3a). The plume area then continues to rise over the next 6.3 h as pore spaces in the hyporheic zone fill with tracer from the stream and the plume disperses (Fig. 3a). At 6.3 h, the tracer plume area abruptly decreases from 10.2 to 9.1 m² due to flushing of freshwater from the stream. With further spreading, tracer concentrations become more diluted within the hyporheic zone, and the plume area continues to decline. After 10 h from the start of the test, the plume area decreases to zero, meaning that σ_h falls within 10% of the background value everywhere in the 2-D transect beneath the electrodes. In comparison, the plume area from σ_{hi} is overestimated during the early part of the injection, when the stream behaves as a highly conductive region (Fig. 3a): the area initially increases to 5.4 m² in the first 15 min. Plume area from $\sigma_{b,i}$ continues to increase during most of the remaining injection period (Fig. 3a). However, plume area from $\sigma_{h,i}$ rapidly contracts after 7 h, when the stream is fully flushed of saline tracer, though the plume area from σ_b continues to

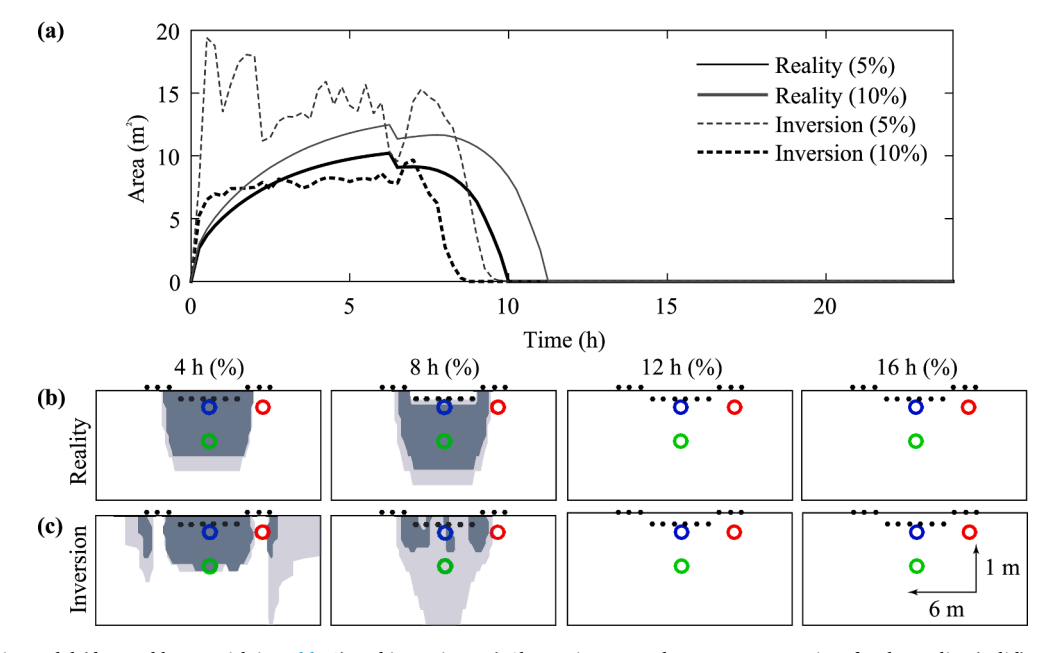


Fig. 3. Base scenario model (denoted by asterisk in Table 1) and inversions. a) Change in tracer plume extent over time for the reality (solid) and as estimated in the inversion (dashed) by a change in bulk EC of 5, and 10%. b) and c) Time series of tracer plume areas based on the 5% and 10% cutoff in reality and inversion.

decline over several more hours (Fig. 3a).

3.2. Stream geometry effects

3.2.1. $\bar{\sigma}_b$ and $\bar{\sigma}_{b,a}$

For streams of different geometry (4×0.1 m, 6×0.2 m, and 8×0.3 m), breakthrough curves for $\bar{\sigma}_{b,a}$ and $\bar{\sigma}_b$ again show very different plateau values during the injection but similar tailing behavior for streams of any size (Fig. 4a, Table 3), especially when compared to the fluid EC.

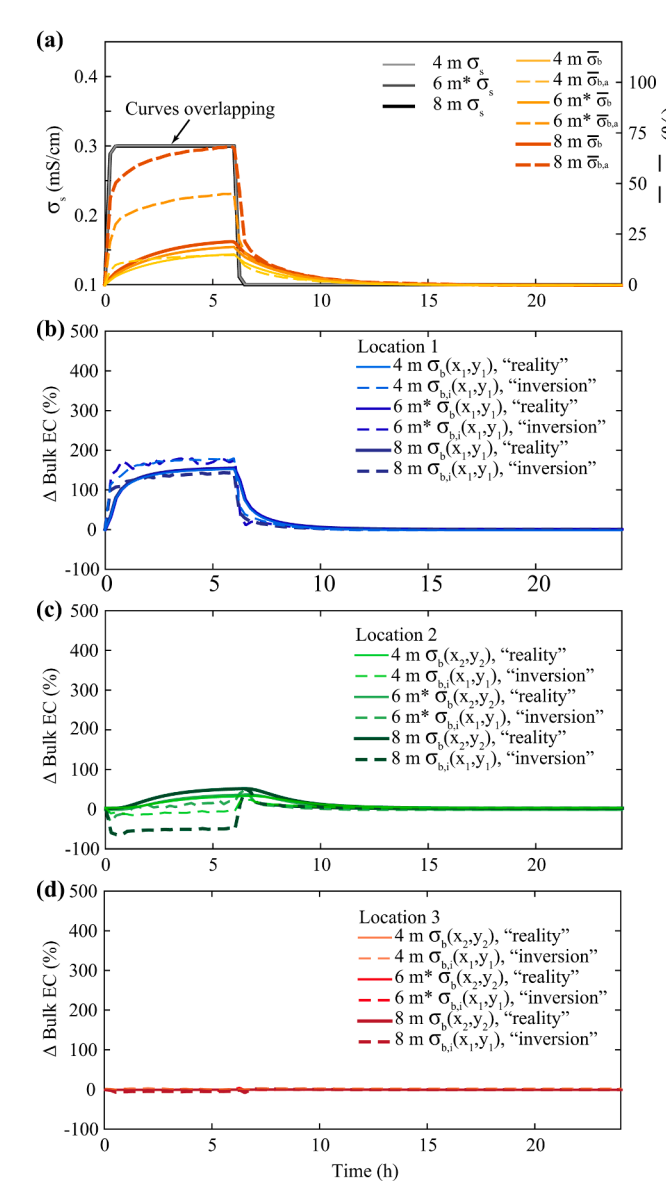


Fig. 4. (a) Time series of stream fluid EC (σ_8) (solid black line, these lines overlap with each other), spatially averaged bulk EC $(\bar{\sigma}_b)$, Eq. (9) over time in a cross-section beneath the electrode transect (solid orange lines) and change in average apparent bulk EC $(\bar{\sigma}_{b,a})$ (Eq. (7), dashed orange lines) for three scenarios with different stream size (Table 1, stream widths of 4, 6, and 8 m, and stream depths of 0.1, 0.2, and 0.3 m, respectively). (b-d) Bulk EC breakthrough curves at locations 1 (b), 2 (c), and 3 (d) for model ("reality", σ_b) and inversion $(\sigma_{b,i})$ for same three scenarios. (e) Change in the tracer plume area through time, defined where bulk EC has increased by at least 10%, for the same three scenarios. The asterisk indicates the 6-m width base scenario. (For interpretation of the references to colour in this figure legend, the reader is referred to the web version of this article.)

3.2.2. Inversions

In the inversions at Location 1 (0.15 m deep in the streambed), the stream geometry has an impact on the $\sigma_{b,i}$ breakthrough curve: in our small stream (less than or equal to 6 m wide), the change in $\sigma_{h,i}$ beneath the stream is overestimated, while in the relatively larger stream (wider than 6 m) (Fig. 4), it is underestimated because of the negative inversion artifact (Fig. S1). The tail in the inversions at Location 1 is consistently underestimated for streams of any size because of smoothing affects in the inversion (Fig. 4b, Table 3). At Location 2 (depth of 0.95 m in the streambed), negative changes in $\sigma_{b,i}$ are particularly severe during the injection period in the case of the larger stream (Fig. 4c). The tail in the inversion is again underestimated at this location for stream of all sizes (Fig. 4c, Table 3). At Location 3 (within the floodplain), the change in σ_b is never more than 1% (Table 3), but $\sigma_{b,i}$ increases above the noise threshold in the smaller streams (4.0% and 4.9% for 4-m and 6-m wide streams, respectively). In other words, the inversion suggests the presence of tracer where only negligible concentrations exist, due again to smoothing in the inversion. However, the inversions generally resolve the overarching patterns of saline tracer migration (Supplementary Fig. S1), with differing impacts from artifacts. The 4-m channel and its hyporheic zone form a smaller target, but the plume is still well resolved (exhibiting roughly a 19.9–178.2% change in $\sigma_{b,i}$ beneath the stream) until late time, around 12 h. In the case of the larger 8-m wide channel, the inversions during the tracer injection period show a particularly large artifact (negative anomaly) at great depth beneath the stream (Supplementary Fig. S1). Comparing the inversion results in 4-, 6-, and 8-m wide streams, the artifact size and magnitude both increase with the stream size in these models. As noted earlier, we did not test changes in stream depth and width separately in an effort to reduce the number of scenarios, since depth and width tend to scale together; however, we can speculate that depth might influence artifacts more than width because it has a more local influence on the electrical conductance between pairs of electrodes in the stream, but increasing either one would increase the volume of electrically conductive surface water that is accessible to current, so both are controlling factors.

3.3. Tracer concentration effects

3.3.1. $\bar{\sigma}_b$ and $\bar{\sigma}_{b,a}$

For changes in stream water EC of 0.2, 0.3, and 0.4 mS cm⁻¹, breakthrough curves for $\bar{\sigma}_{b,a}$ and $\bar{\sigma}_b$ again show good agreement in tailing behavior (Fig. 5a, Table 3), especially when compared to fluid EC.

3.3.2. Inversions

The inversions again resolve the overarching patterns of saline tracer migration (Fig. S2). However, severe negative inversion artifacts occur during the saline tracer injection for greater plateau concentrations (Fig. S2). At Location 1 in the shallow hyporheic zone, the pixel breakthrough curves from $\sigma_{b,i}$ again capture the approximate behavior of σ_b breakthrough curves, but with a faster arrival and shorter tail, regardless of plateau concentration in the stream (Fig. 5b, Table 3). The peak change in σ_b and $\sigma_{b,i}$ during the injection agrees best for the dilute injection (0.2 mS cm⁻¹) (Fig. 5b, Table 3). At Location 2 (Fig. 5c), agreement in the peak change is again best for the dilute injection, but the tails in the inversion are consistently underestimated for all injection scenarios (Table 3). At Location 3, $\sigma_{b,i}$ increases above the 2% noise threshold for all scenarios, even though σ_b in "reality" at this location does not (Fig. 5c, Table 3).

3.4. Tracer injection interval effects

3.4.1. $\bar{\sigma}_b$ and $\bar{\sigma}_{b,a}$

For tracer injection times of 4, 6, and 8 h, the tails in $\bar{\sigma}_{b,a}$ are again similar in character to the tails in $\bar{\sigma}_b$ (Fig. 6a) when compared to fluid EC.

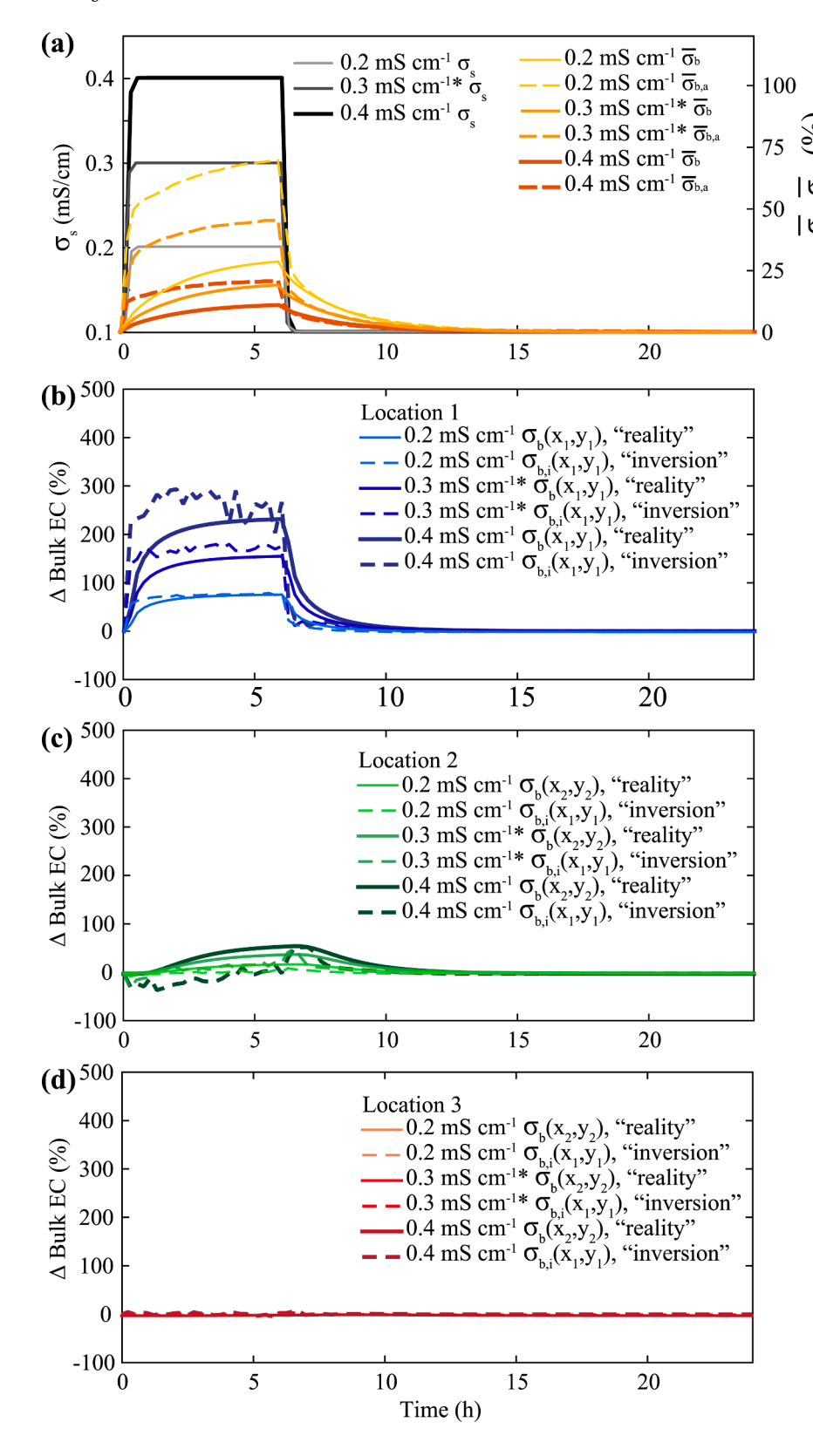


Fig. 5. (a) Time series of stream fluid EC (ns) (solid black line), spatially averaged bulk EC ($\bar{\sigma}_b$, Eq. (9) over time in a cross-section beneath the electrode transect (solid orange lines) and change in average apparent bulk EC ($\bar{\sigma}_{b,a}$) (Eq. (7), dashed orange lines) for three scenarios with different plateau tracer concentrations (Table 1, change in stream fluid EC of 0.2, 0.3, and 0.4 mS $\rm cm^{-1}$). (b-d) Bulk EC breakthrough curves at locations 1 (b), 2 (c), and 3 (d) for model ("reality", σ_b) and inversion ($\sigma_{b,i}$) for same three scenarios. (e) Change in the tracer plume area through time, defined where bulk EC has increased by at least 10%, for the same three scenarios. The asterisk indicates the base scenario with EC of 0.3 mS cm⁻¹ in stream fluid EC. (For interpretation of the references to colour in this figure legend, the reader is referred to the web version of this article.)

3.4.2. Inversions

The inversions again resolve the general patterns of saline tracer migration (Fig. S3). At the end of the longest injection period (8 h), the inversion suggests a substantial increase in $\sigma_{b,i}$ in the floodplain (along the stream sides) that does not exist in the synthetic system (Fig. S3).

For injections of any length, peak changes in $\sigma_{b,i}$ at the three loca-

tions in the inversion and the synthetic system are all similar (Fig. 6b – d). For example, at Location 1 (Fig. 6b), the peak change in EC in the synthetic system is 178% for the 4-hour injection, while the peak change is 181% for the 8-hour injection (Fig. 6b), which matches the peak change in $\sigma_{b,i}$. For all three scenarios, $\sigma_{b,i}$ again declines too rapidly after the injection at Location 1, relative to the synthetic system. At Location

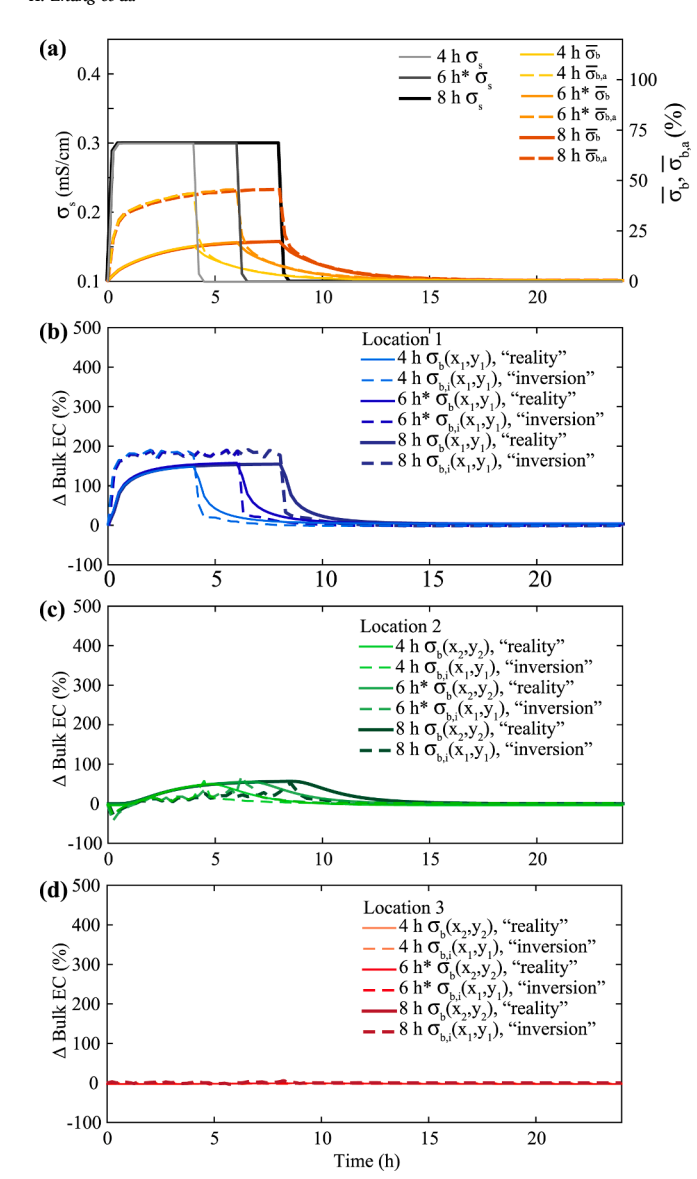


Fig. 6. (a) Time series of stream fluid EC ($_{\sigma s}$) (solid black line, the two lines overlap with each other), spatially averaged bulk EC ($\bar{\sigma}_b$, Eq. (9) over time in a cross-section beneath the electrode transect (solid orange lines) and change in average apparent bulk EC ($\bar{\sigma}_{b,a}$) (Eq. (7), dashed orange lines) for three scenarios with different injection periods (Table 1, injection lengths of 4 h, 6 h, and 8 h). (b-d) Bulk EC breakthrough curves at locations 1 (b), 2 (c), and 3 (d) for model ("reality", σ_b) and inversion ($\sigma_{b,i}$) for same three scenarios. (e) Change in the tracer plume area through time, defined where bulk EC has increased by at least 10%, for the same three scenarios. The asterisk indicates the base scenario with 6 h injection. (For interpretation of the references to colour in this figure legend, the reader is referred to the web version of this article.)

2, $\sigma_{b,i}$ is generally underestimated at most times, particularly in the tail, for all three injection-length scenarios. At Location 3, $\sigma_{b,i}$ again changes more than σ_b (peaks of 5.9, 4.9, and 5.8% in the inversion compared with peaks of 0.5, 0.6, and 0.7% in the synthetic system for injection times of 4, 6, and 8 h).

3.5. Heterogeneity effects

3.5.1. $\bar{\sigma}_b$ and $\bar{\sigma}_{b,a}$

The net effect of heterogeneity is to slightly increase the time that the saline tracer lingers in the subsurface ($\bar{\sigma}_b$ returns to within 2% of background after 11.0 h instead of 10.7 for the base case in Table 3 and Fig. 7a). Interestingly, $\bar{\sigma}_{b,a}$ does not reflect this heavier tailing behavior

(Fig. 7a): the time to recover to within 2% of background is actually 0.3 h shorter for the heterogeneous case than the homogeneous case (compare dashed lines in Fig. 7a, Table 3). Heterogeneity likely holds onto solute in the subsurface more than a homogeneous system, but this mass may be "lost" to the ER and not clearly detected (Fig. 7a). In other words, heterogeneity changes the distribution of saline tracer in the subsurface only slightly as simulated here. As in the homogeneous case, the tail in $\bar{\sigma}_{b,a}$ is similar to the tail in $\bar{\sigma}_b$, but the peak changes do not agree very well (Fig. 7a, Table 3).

3.5.2. Inversions

For heterogeneous sediments with bimodally distributed permeabilities, the saline tracer plume in the synthetic system is more irregular in shape, following connected pathways along zones of greater permeability (Fig. S4). The inversions capture the general evolution of the plume but miss some irregularities in the plume shape due to limited resolution and smoothing, so again underestimate the concentration of tracer at late time (Fig. S4). At the three pixel locations of interest, $\sigma_{b,i}$ curves show little difference between homogeneous and heterogeneous cases (Fig. 7b – d, Table 3). In contrast, differences in σ_b for the synthetic heterogeneous and homogeneous systems are slightly greater, particularly at Locations 1 and 2 (Fig. 7b – d. Table 3). For example, at Location 1 in the shallow hyporheic zone, the synthetic system has a peak change in σ_h of 176% in heterogenous case versus 151% in homogenous one, but both $\sigma_{b,i}$ show a peak change of 186%. Similarly, at Location 2, the heterogeneous synthetic system has a longer tail than the homogeneous one (σ_b returns to 2% of its background value after 15 and 13 h, respectively, but $\sigma_{b,i}$ returns to 2% of its background value after 9.7 and 10.2 h (Fig. 7c). $\sigma_{b,i}$ noticeably underestimates variations in σ_b caused by heterogeneity in permeability (Table 3).

4. Discussion

4.1. Insights from synthetic models

4.1.1. $\bar{\sigma}_b$ and $\bar{\sigma}_{b,a}$

Changes in $\bar{\sigma}_{b,a}$ (as "measured" in ER surveys) and $\bar{\sigma}_b$ within the synthetic system (the "reality") both decreased to within 2% of the background value over similar times. The closest agreement in this tailing behavior occurred for the smaller (4-m) stream with dilute injection (0.2 mS cm⁻¹) (Fig. 4a, Fig. 6a, and Fig. 7a), suggesting that $\bar{\sigma}_{b,a}$ can be a valuable calculation for capturing the tail of the saline tracer passage. It is important to remember, however, that $\bar{\sigma}_{b,a}$ curves are not spatially explicit—they have a large support volume beneath the electrode transect and are sensitive to solute well outside of the single-plane calculation done here. Thus, the $\bar{\sigma}_{b,a}$ curve is useful for quantifying timescales of saline tracer plume passage and retention rather than magnitudes of concentration changes in any part of the transect. For example, the recovery time for $\bar{\sigma}_b$ and $\bar{\sigma}_{b,a}$ to return to within 2% of the background value is 10.7 and 11.0 h for the base case scenario, though their peak values are quite different (Fig. 2a, Table 3). The $\bar{\sigma}_{b,a}$ curves can also be used, prior to inversion, to determine whether one would expect detectable changes to be present in an inversion—if there are no changes in $\bar{\sigma}_{b,a}$ above noise, then the inversion will not show meaningful changes either, and there is no point inverting data that do not show changes.

4.1.2. Inversions

In contrast, inversions offer highly desirable, spatially distributed maps with information on solute transport, but are prone to artifacts (Fig. 2d, Figs. S1 – S4). Hyporheic tracer-test applications are mathematically challenging for inversion because the hyporheic zone is an inherently thin target overlain by a highly electrically conductive stream (note strong contrasts in σ_b near the stream in the background model, Fig. 2). In inversions, $\sigma_{b,i}$ changes in the stream will bleed into pixels in

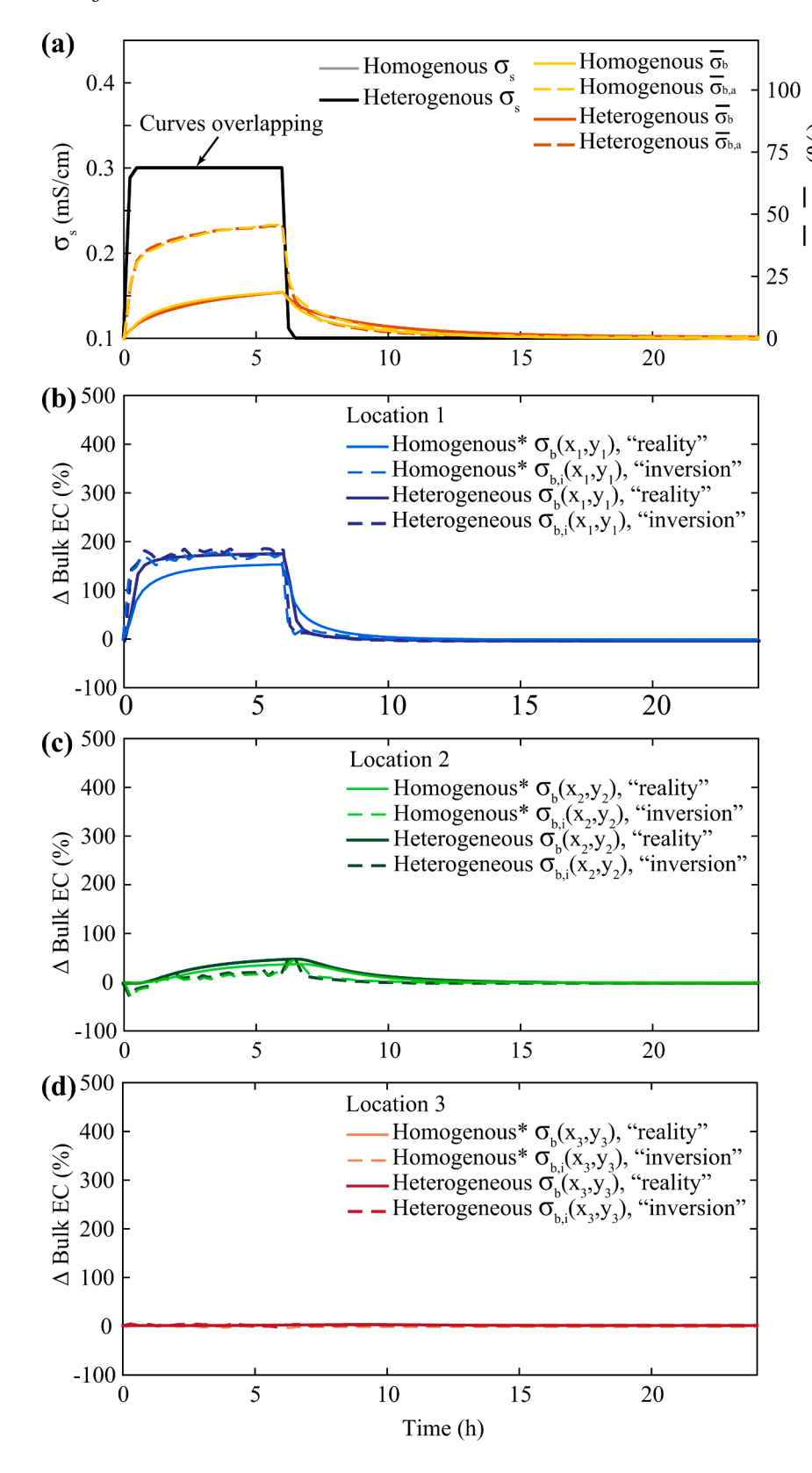


Fig. 7. (a) Stream fluid EC (σ_s), spatially averaged bulk EC ($\bar{\sigma}_b$, Eq. (9) in the synthetic stream system, and average apparent bulk EC ($\bar{\sigma}_{b,a}$) (Eq. (7), dashed orange lines) for two scenarios with homogenous and heterogenous K (Table 1). (b-d) Bulk EC breakthrough curves at locations 1 (b), 2 (c), and 3 (d) for model ("reality", σ_b) and inversion ($\sigma_{b,i}$) for the same three scenarios. (e) Change in plume tracer area through time. Asterisk indicates the homogeneous aquifer scenario. (For interpretation of the references to colour in this figure legend, the reader is referred to the web version of this article.)

the hyporheic zone and surrounding aquifer during the injection period (e.g., inversion at 4 h in Fig. 2d) without a regularization constraint separating one from the other. Thus, changes in $\sigma_{b,i}$ and saline tracer plume area from $\sigma_{b,i}$ are prone to gross overestimation compared to reality, as tracer appears to extend beyond the stream prior to its actual

arrival. Sawyer et al. (2015) noted similar issues resolving the appearance of tracer in a karst conduit, where the tracer plume appeared larger and more diffuse than borehole observations suggested. Without separating the stream from the subsurface in inversions, the inversions may not yield reliable estimations of $\sigma_{b,i}$ in the subsurface during the injection period. Inversions should not be interpreted for quantitative areas

of saline tracer penetration beneath the stream in any regard, but the impact of tracer area or volume on measurements and subsequent inversions can be explored with forward models, at least in a synthetic sense. Another complicating factor is that 2-D inversions squeeze the three-dimensionality of flow and transport into a single plane (e.g., Nimmer et al. (2008)), which can create the illusion of the tracer arriving early, as an electrically conductive tracer approaches the transect from upstream. This out-of-plane effect has been noted in previous field tracer studies (e.g., Ward et al., 2010). It is less of an issue here—we can be confident that the "early" appearance of saline tracer beneath the streambed is mainly due to aforementioned smoothing of the EC anomaly in the stream) for the following reason: the saline tracer moves rapidly downstream relative to the 15-minute interval for synthetic time-lapse ER "measurements." Specifically, the advective travel distance of saline tracer in the stream over one 15-minute sequence is 90 m ($v_s = 0.1 \text{ m s}^{-1}$, Table 2) suggesting that the saline tracer plume fills the stream over the entire experimental reach in much less than one survey interval. The implication is that only one snapshot in the time series is subject to potentially large out-of-plane effects as the injection begins (and similarly only one snapshot as the injection ends).

While inversions tend to overestimate $\sigma_{b,i}$ immediately below the stream (e.g., Location 1) during injections, they can underestimate $\sigma_{b,i}$ much deeper below the stream (e.g., Location 2) due to smoothing around zones of abrupt change in $\sigma_{b,i}$ such as the sediment-water interface and base of the saline plume within the hyporheic zone. Many of our inversions also show artifacts in the stream banks that appear like dipoles of neighboring positive and negative changes in $\sigma_{b,i}$. These zones of overestimation and underestimation emerge near sharp contrasts in σ_b due to minimization of the second derivative during regularization and are also apparent in field studies, e.g. Fig. 6 in Clemence et al. (2017) and Fig. 2 in Ward et al. (2010a). By minimizing the 2nd derivative—trying to keep the curvature small rather than the slope—the inversion changes the slope and creates overshoots and undershoots associated with the estimated field.

4.2. Recommendations

Our results suggest that injecting saline tracers at modest concentration in streams is likely to produce a better target for hyporheic imaging, namely a plume with smaller gradients in σ_b . For example, the scenario with an 6-m wide stream and a 100% change (2-fold increase) in stream fluid EC had the smallest discrepancies between $\sigma_{b,i}$ and σ_b in Location 1 (Figs. 2 and 3). In field applications, the differences between stream EC before and during the plateau have often been on the order of 3-fold increase (Doughty et al., 2020; Menichino et al., 2014; Doetsch et al., 2012; Ward et al., 2010b). It is fortuitous that lower concentrations are better suited for resolving hyporheic transport, as more labor is needed to inject more salt, as discussed further below, especially in larger streams.

The "optimal" injection period and plateau tracer concentration depend on the flow paths of interest and are site-specific (e.g., González-Pinzón et al., 2022), related to each site's unique system. Our results show that a shorter injection period (in this case, 4 h) may not be sufficient to introduce enough salt to the hyporheic zone to aid detection at later times (Supplementary Fig. 3), suggesting that a longer injection period at low concentration is best for resolving hyporheic transport. Even if optimal injection periods and plateau tracer concentrations could be known or estimated for every site at a given time, it would not necessarily be practical to inject the required amount of tracer over the optimal time period. For example, at some sites without road access, the mass of tracers that can be carried in on foot exerts a practical constraint.

This study also suggests that ER inversions in larger streams may be more prone to artifacts, as observed in the 8-m wide stream scenario (Fig. 4). Ideally, smaller streams with bigger hyporheic zones are more ideal for ER imaging (both in terms of minimizing the impact of the

stream in the inversions and resolving tracer plume migration), but hyporheic size may scale with stream size, up to a point (Hester and Doyle, 2008). Most field applications have utilized small streams, generally <10 m wide (Table 1). This small size is partially due to a common research focus on headwater streams but also due to the practical challenge of adding enough salt to large rivers to resolve changes in σ_b within the subsurface. In two cases where time-lapse ER methods were applied to large rivers, Cardenas and Markowski (2011) and Coscia et al. (2011) took advantage of natural changes in river discharge to image the movement of the mixing interface between river water and groundwater rather than adding tracers.

These synthetic experiments are useful for creating guidelines for interpreting time-lapse ER surveys of stream tracer tests:

- 1) The injection period is generally a time when ER measurements inadequately resolve changes in σ_b nearest the stream due to severe artifacts that obscure tracer transport in the hyporheic zone. While we did not explore it here, specifying the stream bathymetry and concentration directly in inversions and decoupling the regularization across the aquifer system to the stream can improve inversions (Coscia et al., 2011). While fluid EC is easy to monitor, estimating stream bathymetry (and then introducing it into numerical models) can be difficult for shallow, rocky-bedded streams. Inversions are most reliable when the steep gradients in σ_b that present problems for ER are mostly dissipated—so at late time during tracer tests, as long as changes in σ_b remain above the noise threshold. While tracer concentrations in the stream are elevated during injection, smoothing effects and artifacts may be most apparent, meaning that high tracer concentrations in the hyporheic zone and stream may be most severely underestimated in the inversion, and low values most severely overestimated (the tracer appears to extend over a larger area than it does in reality) (Supplementary Fig. 1).
- 2) Pixels at intermediate distance from the stream may be more likely to yield reliable breakthrough information. The locations of best-resolved pixels will vary with the geometry and electrical conductivity of the stream and hyporheic zone, as well as electrode positions and geometry used to collect data on those electrodes. For example, the most reliable information was often between Locations 1 and 2 in this synthetic study as could be mapped with a resolution matrix (e. g., Day-Lewis et al., 2005). It is worth noting that pixel breakthrough curves are a complimentary analysis but not a replacement for monitoring breakthrough curves at specific locations in the subsurface (for example, using a piezometer and fluid electrical conductivity sensor) when possible (e.g. Houzé et al., 2022). We recognize, however, that in many headwater streams, the rocky nature of the streambed can make it difficult to install such monitoring points (e.g. Doughty et al., 2020).
- 3) Plume areas estimated from ER is not reliable because of smoothing in the inversions; moment-based analyses may be one way forward if plume areas are the primary interest (Pidlisecky et al, 2011).
- 4) We recommend calculating $\bar{\sigma}_{b,a}$ for all tracer data sets as it does not require inversion and is an indicator of lingering tracer in the hyporheic zone after the passage of tracer in the stream, and also determines whether inversions are worth conducting. If $\bar{\sigma}_{b,a}$ does not change over time during salt injection experiment, ER surveyed data is invalid and there is no need to do an inversion for this data set. A downside of $\bar{\sigma}_{b,a}$ is that it lacks spatial information inherent in ER inversions and represents a blended measure of tracer transport in the stream and subsurface.

It is also worth noting that ER offers important information to the stream community that can be used to make decisions during tracer tests. For example, a common concern is whether an injection has proceeded long enough for saline tracer to penetrate hyporheic flow paths of interest and return to the stream, often referred to as the "window of

detection" issue (Harvey and Bencala, 1993; Wagner and Harvey, 1997; Harvey and Wagner, 2000). ER measurements, particularly of $\bar{\sigma}_{b,a}$, may provide a tool that can be used in real -time or near-real time to explore when most of the tracer has returned from the hyporheic zone to the stream.

4.3. Limitations of this study

Our study uses a simplified conceptualization of hyporheic flow and solute transport to test the capability and resolution of ER for hyporheic zone detection. Heterogeneities in stream properties such as width, length, slope, meanders, bathymetric roughness, sediment hydraulic properties, gaining or losing conditions, and turbulence all have an impact on hyporheic flow and the transport of electrically conductive solutes through the hyporheic zone. In field systems, other properties may impact ER data that we did not consider here, including temperature, moisture content, location of the water table, and temporal smearing. Changing one or several of these factors would change the hyporheic exchange zone and/or affect the ER inversion results (Hinnell et al., 2010).

In this study, we only tested one ER transect configuration (perpendicular to the stream). Transects could also be positioned along the thalweg inside the stream, for example, and in this case, artifacts beneath the stream and out-of-plane effects would be expected to differ. In particular, changes in artifacts due to variations in stream depth along a stream-parallel profile could incorrectly be interpreted as changes in the depth of saline tracer mixing. Other aspects of ER survey design (for example, electrode spacing and ER profile length) also determine the inversion outputs and were not examined here but have been addressed in other studies (Ward et al., 2010b). In field applications, designs are constrained by what is suitable for site conditions. For example, large rivers would require a long ER profile, and braided streams may need small electrode spacing. A small electrode spacing and long survey profile certainly provide more information and resolution for the output results.

5. Conclusions

The application of time-lapse electrical resistivity methods to hyporheic zone studies has rapidly advanced, and a variety of approaches exist to analyze the data. This study explored how differing field characteristics might be interpreted from ER data by creating synthetic stream and hyporheic systems using coupled, three-dimensional fluid flow, solute transport, and electricity conduction models. In cases of small streams where regularization was coupled across the streamaquifer boundary as explored here, we found that inversions tend to overestimate the change in σ_b within the hyporheic zone immediately beneath the stream while saline tracer is present in the stream and underestimate σ_b at late times when the saline tracer is more dilute. The amount of smoothing and size of discrepancies between "reality" and the subsequent inversions change under different stream depths and widths, tracer concentrations and injection periods, and scenarios of aquifer heterogeneity. Generally, we find that there is such a thing as injecting too much tracer: some inversion artifacts can be minimized by maintaining lower spatial gradients in σ_b by injecting at lower concentrations. Discrepancies between $\sigma_{b,i}$ and σ_b (both in terms of peak change and the time for recovery to background) may be minimized for small streams with relatively large hyporheic zones and relatively homogeneous sediments. The time series of $\bar{\sigma}_{b,a}$ measured at electrodes requires no inversion and generally appears to better detect lingering tracer in the hyporheic zone compared with pixel breakthrough curves in the inversion and may be useful in thinking about the "window of detection" problem that occurs with tracer tests. Our analysis also suggests that tracer plume areas cannot be reliably interpreted from inversions due to smoothing.

Declaration of Competing Interest

The authors declare that they have no known competing financial interests or personal relationships that could have appeared to influence the work reported in this paper.

Data availability

The input files of the numerical model and R2 inversion are available online: https://doi.org/10.5281/zenodo.7894414.

Acknowledgments

This research was supported by the National Science Foundation (EAR-1819086 & EAR-1819134). We thank three anonymous reviewers for their comments that improved the manuscript.

Appendix A. Supplementary data

Supplementary data to this article can be found online at https://doi.org/10.1016/j.jhydrol.2023.129577.

References

- Allen, G.H., Pavelsky, T.M., Barefoot, E.A., Lamb, M.P., Butman, D., Tashie, A., Gleason, C.J., 2018. Similarity of stream width distributions across headwater systems. Nat Commun 9 (1). https://doi.org/10.1038/s41467-018-02991-w.
- Bethune, J., Randell, J., Runkel, R.L., Singha, K., 2015. Non-invasive flow path characterization in a mining-impacted wetland. J. Contam. Hydrol. 183, 29–39. https://doi.org/10.1016/j.jconhyd.2015.10.002.
- Binley, A., Kemna, A., 2005. DC resistivity and induced polarization methods, in Hydrogeophysics. In: Rubin, Y., Hubbard, S.S. (Eds.), Water Science and Technology LibraryHydrogeophysics. Springer Netherlands, Dordrecht, pp. 129–156.
- Boano, F., Revelli, R., Ridolfi, L., 2008. Reduction of the hyporheic zone volume due to the stream-aquifer interaction. Geophys. Res. Lett. 35, L09401. https://doi.org/ 10.1029/2008GL033554.
- Bryant, S.R., Sawyer, A.H., Briggs, M.A., Saup, C.M., Nelson, A.R., Wilkins, M.J., Christensen, J.N., Williams, K.H., 2020. Seasonal manganese transport in the hyporheic zone of a snowmelt-dominated river (East River, Colorado, USA). Hydrogeology Journal 28 (4), 1323–1341. https://doi.org/10.1007/s10040-020-02146-6.
- Busato, L., Boaga, J., Perri, M.T., Majone, B., Bellin, A., Cassiani, G., 2019.
 Hydrogeophysical characterization and monitoring of the hyporhetic and riparian zones: The Vermigliana Creek case study. Science of the Total Environment 648, 1105–1120. https://doi.org/10.1016/j.scitotenv.2018.08.179.
- Cardenas, M.B., Markowski, M.S., 2011. Geoelectrical Imaging of Hyporheic Exchange and Mixing of River Water and Groundwater in a Large Regulated River. Environmental Science & Technology 45 (4), 1407–1411. https://doi.org/10.1021/ es103438a.
- Clemence, H., Marc, P., Veronique, D., Toihir, A., 2017. Monitoring an artificial tracer test within streambed sediments with time lapse underwater 3D ERT. Journal of Applied Geophysics 139, 158–169. https://doi.org/10.1016/j.jappgeo.2017.02.003.
- Coscia, I., Greenhalgh, S.A., Linde, N., Doetsch, J., Marescot, L., Guenther, T., Vogt, T., Green, A.G., 2011. 3D crosshole ERT for aquifer characterization and monitoring of infiltrating river water. Geophysics 76 (2), G49–G59. https://doi.org/10.1190/ 1.2552002
- Daily, W., Ramirez, A., 1995. Electrical-Resistance Tomography During In-Situ Trichloroethylene Remediation at the Savanna River Site. Journal of Applied Geophysics 33 (4), 239–249. https://doi.org/10.1016/0926-9851(95)00003-k.
- Day-Lewis, F.D., Singha, K., Binley, A.M., 2005. Applying petrophysical models to radar travel time and electrical resistivity tomograms: Resolution-dependent limitations, *J. Geophys. Res.-Solid.* Earth 110 (B8). https://doi.org/10.1029/2004jb003569.
- Dehkordy, F.M., Briggs, M.A., Day-Lewis, F.D., Singha, K., Krajnovich, A., Hampton, T.B., Zarnetske, J.P., Scruggs, C., Bagtzoglou, A.C., 2019. Multi-scale preferential flow processes in an urban streambed under variable hydraulic conditions. Journal of Hydrology 573, 168–179. https://doi.org/10.1016/j.jhydrol.2019.03.022.
- Doetsch, J., Linde, N., Vogt, T., Binley, A., Green, A.G., 2012. Imaging and quantifying salt-tracer transport in a riparian groundwater system by means of 3D ERT monitoring. Geophysics 77 (5), B207–B218. https://doi.org/10.1190/geo2012-
- Doughty, M., Sawyer, A.H., Wohl, E., Singha, K., 2020. Mapping Increases in Hyporheic Exchange from Channel-Spanning Logjams. Journal of Hydrology 124931. https://doi.org/10.1016/j.jhydrol.2020.124931.
- Elliott, A.H., Brooks, N.H., 1997. Transfer of nonsorbing solutes to a streambed with bed forms: Theory. Water Resour. Res. 33 (1), 123–136. https://doi.org/10.1029/ 96WR02784.
- Gonzalez-Pinzon, R., Ward, A.S., Hatch, C.E., Wlostowski, A.N., Singha, K., Gooseff, M. N., Haggerty, R., Harvey, J.W., Cirpka, O.A., Brock, J.T., 2015. A field comparison of

- multiple techniques to quantify groundwater-surface-water interactions. Freshw. Sci. $34\ (1), 139-160.\ https://doi.org/10.1086/679738.$
- Gooseff, M.N., Anderson, J.K., Wondzell, S.M., LaNier, J., Haggerty, R., 2006. A modelling study of hyporheic exchange pattern and the sequence, size, and spacing of stream bedforms in mountain stream networks, Oregon, USA. Hydrol. Process. 20 (11), 2443–2457. https://doi.org/10.1002/hyp.6349.
- Hakenkamp, C.C., Valett, H.M., Boulton, A.J., 1993. Perspectives on the hyporheic zone: Integrating hydrology and biology. Concluding remarks, J. N. Am. Benthol. Soc. 12 (1), 94–99.
- Hammett, S., Day-Lewis, F.D., Trottier, B., Barlow, P.M., Briggs, M.A., Delin, G., Harvey, J.W., Johnson, C.D., Lane Jr, J.W., Rosenberry, D.O., Werkema, D.D., 2022. GW/SW-MST: A Groundwater/Surface-Water Method Selection Tool. Groundwater 60, 784–791. https://doi.org/10.1111/gwat.13194.
- Harvey, J.W., Wagner, B.J., Bencala, K.E., 1996. Evaluating the reliability of the stream tracer approach to characterize stream-subsurface water exchange. Water Resources Research 32 (8), 2441–2451.
- Hester, E.T., Doyle, M.W., 2008. In-stream geomorphic structures as drivers of hyporheic exchange. Water Resources Research 44 (3).
- Hinnell, A.C., Ferré, T.P.A., Vrugt, J.A., Huisman, J.A., Moysey, S., Rings, J., Kowalsky, M.B., 2010. Improved extraction of hydrologic information from geophysical data through coupled hydrogeophysical inversion, Water Resour. Res. 46, W00D40. https://doi.org/10.1029/2008WR007060.
- Houzé, C., Durand, V., Mügler, C., Pessel, M., Monvoisin, G., Courbet, C., Noûs, C., 2022. Combining experimental and modelling approaches to monitor the transport of an artificial tracer through the hyporheic zone. Hydrological Processes 36 (2), e14498.
- Johnson, T., Versteeg, R., Thomle, J., Hammond, G., Chen, X.Y., Zachara, J., 2015. Four-dimensional electrical conductivity monitoring of stage-driven river water intrusion: Accounting for water table effects using a transient mesh boundary and conditional inversion constraints. Water Resources Research 51 (8), 6177–6196. https://doi.org/10.1002/2014wr016129.
- Knapp, J.L.A., Gonzalez-Pinzon, R., Drummond, J.D., Larsen, L.G., Cirpka, O.A., Harvey, J.W., 2017. Tracer-based characterization of hyporheic exchange and benthic biolayers in streams. Water Resources Research 53 (2), 1575–1594. https://doi.org/10.1002/2016wr019393.
- LaBrecque, D. J., and X. Yang (2001), Difference Inversion of ERT Data: A Fast Inversion Method for 3-D In-Situ Monitoring, in Symposium on the Application of Geophysics to Engineering and Environmental Problems 2000, edited, 907-914 pp.
- Larson, L.N., Fitzgerald, M., Singha, K., Gooseff, M.N., Macalady, J.L., Burgos, W., 2013. Hydrogeochemical niches associated with hyporheic exchange beneath an acid mine drainage-contaminated stream. Journal of Hydrology 501, 163–174. https://doi. org/10.1016/j.jibydrol.2013.08.007.
- Lewandowski, J., Meinikmann, K., Krause, S., 2020. Groundwater-Surface Water
 Interactions: Recent Advances and Interdisciplinary Challenges. Water 12 (1), 296.
- McLachlan, P., Blanchy, G., Binley, A., 2021. EMagPy: Open-source standalone software for processing, forward modeling and inversion of electromagnetic induction data. Computers and Geosciences 146, 104561.
- Menichino, G.T., Ward, A.S., Hester, E.T., 2014. Macropores as preferential flow paths in meander bends. Hydrol. Process. 28 (3), 482–495. https://doi.org/10.1002/hyp.9573
- COMSOL Multiphysics. (2019). Introduction to COMSOL multiphysics. Version 5.5. COMSOL. Burlington, MA.
- Nimmer, R.E., Osiensky, J.L., Binley, A.M., Williams, B.C., 2008. Three-dimensional effects causing artifacts in two-dimensional, cross-borehole, electrical imaging. Journal of Hydrology 359 (1–2), 59–70.
- Pidlisecky, A., Singha, K., Day-Lewis, F.D., 2011. A distribution-based parameterization for improved tomographic imaging of solute plumes. Geophysical Journal International 187 (1), 11 p. https://doi.org/10.1111/j.1365-246X.2011.05131.x.
- International 187 (1), 11 p. https://doi.org/10.1111/j.1365-246X.2011.05131.x. Sawyer, A.H., Zhu, J.F., Currens, J.C., Atcher, C., Binley, A., 2015. Time-lapse electrical resistivity imaging of solute transport in a karst conduit. Hydrol. Process. 29 (23), 4968-4976. https://doi.org/10.1002/hyp.10622.

- Singha, K., Gorelick, S.M., 2005. Saline tracer visualized with three-dimensional electrical resistivity tomography: Field-scale spatial moment analysis. Water Resources Research 41 (5). https://doi.org/10.1029/2004wr003460.
- Singha, K., Day-Lewis, F.D., Lane, J.W., 2007. Geoelectrical evidence of bicontinuum transport in groundwater. Geophys. Res. Lett. 34 (12) https://doi.org/10.1029/ 2007gl030019.
- Smidt, S.J., Cullin, J.A., Ward, A.S., Robinson, J., Zimmer, M.A., Lautz, L.K., Endreny, T. A., 2015. A Comparison of Hyporheic Transport at a Cross-Vane Structure and Natural Riffle. Groundwater 53 (6), 859–871. https://doi.org/10.1111/gwat.12288.
- Sparacino, M.S., Rathburn, S.L., Covino, T.P., Singha, K., Ronayne, M.J., 2019. Form-based river restoration decreases wetland hyporheic exchange: Lessons learned from the Upper Colorado River. Earth Surface Processes and Landforms 44 (1), 191–203. https://doi.org/10.1002/esp.4525.
- Stonedahl, S.H., Harvey, J.W., Wörman, A., Salehin, M., Packman, A.I., 2010.

 A multiscale model for integrating hyporheic exchange from ripples to meanders.

 Water Resour. Res. 46, W12539. https://doi.org/10.1029/2009WR008865.
- Toran, L., Hughes, B., Nyquist, J., Ryan, R., 2012. Using Hydrogeophysics to Monitor Change in Hyporheic Flow around Stream Restoration Structures. Environ. Eng. Geosci. 18 (1), 83–97. https://doi.org/10.2113/gseegeosci.18.1.83.
- Toran, L., Nyquist, J.E., Fang, A.C., Ryan, R.J., Rosenberry, D.O., 2013. Observing lingering hyporheic storage using electrical resistivity: variations around stream restoration structures, Crabby Creek, PA. Hydrol. Process. 27 (10), 1411–1425. https://doi.org/10.1002/hyp.9269.
- Triska, F.J., Duff, J.H., Avanzino, R.J., 1993. Patterns of hydrological exchange and nutrient transformation in the hyporheic zone of a gravel-bottom stream: examining terrestrial-aquatic linkages. Freshwater Biology 29 (2), 259–274.
- Ward, A.S., Gooseff, M.N., Singha, K., 2010a. Imaging hyporheic zone solute transport using electrical resistivity. Hydrol. Process. 24 (7), 948–953. https://doi.org/ 10.1002/hyp.7672.
- Ward, A.S., Gosseff, M.N., Singha, K., 2010b. Characterizing hyporheic transport processes - Interpretation of electrical geophysical data in coupled stream-hyporheic zone systems during solute tracer studies. Adv. Water Resour. 33 (11), 1320–1330. https://doi.org/10.1016/j.advwatres.2010.05.008.
- Ward, A.S., Fitzgerald, M., Gooseff, M.N., Voltz, T.J., Binley, A.M., Singha, K., 2012. Hydrologic and geomorphic controls on hyporheic exchange during base flow recession in a headwater mountain stream. Water Resources Research 48 (W04513). https://doi.org/10.1029/2011wr011461.
- Ward, A.S., Gooseff, M.N., Fitzgerald, M., Voltz, T.J., Singha, K., 2014. Spatially distributed characterization of hyporheic solute transport during baseflow recession in a headwater mountain stream using electrical geophysical imaging. Journal of Hydrology 517, 362–377. https://doi.org/10.1016/j.jhydrol.2014.05.036.
- White, D.S., 1993. Perspectives on defining and delineating hyporheic zones. J. N. Am. Benthol. Soc. 12 (1), 61–69.
- Wilkinson, P.B., Meldrum, P.I., Chambers, J.E., Kuras, O., Ogilvy, R.D., 2006. Improved strategies for the automatic selection of optimized sets of electrical resistivity tomography measurement configurations. Geophysical Journal International 167 (3), 1119–1126. https://doi.org/10.1111/j.1365-246X.2006.03196.x.
- Winter, T.C., Harvey, J.W., Franke, O.L., Alley, W.A., 1998. Groundwater and surface water: A single resource, U.S. Geological Survey Circular 1139, 1–79.
- Woessner, W.W., 2000. Stream and fluvial plain ground water interactions: Rescaling hydrogeologic thought. Ground Water 38 (3), 423–429.
- Wondzell, S.M., Swanson, F.J., 1996. Seasonal and storm dynamics of the hyporheic zone of a 4th-order mountain stream. 2. Nitrogen cycling. Journal of the North American Benthological Society 15 (1), 20–34. https://doi.org/10.2307/1467430
- Benthological Society 15 (1), 20–34. https://doi.org/10.2307/1467430. Wroblicky, G.J., Campana, M.E., Valett, H.M., Dahm, C.N., 1998. Seasonal variation in surface-subsurface water exchange and lateral hyporheic area of two stream-aquifer systems. Water Resources Research 34 (3), 317–328.